

# Polarimetric Microwave Wind Radiometer Model Function and Retrieval Testing for WindSat

Simon H. Yueh, *Senior Member, IEEE*, William J. Wilson, *Fellow, IEEE*, Steve J. Dinardo, *Member, IEEE*, and S. Vincent Hsiao

**Abstract**—A geophysical model function (GMF), relating the directional response of polarimetric brightness temperatures to ocean surface winds, is developed for the WindSat multifrequency polarimetric microwave radiometer. This GMF is derived from the WindSat data and tuned with the aircraft radiometer measurements for very high winds from the Hurricane Ocean Wind Experiment in 1997. The directional signals in the aircraft polarimetric radiometer data are corroborated by coincident Ku-band scatterometer measurements for wind speeds in the range of 20–35 m/s. We applied an iterative retrieval algorithm using the polarimetric brightness temperatures from 18-, 23-, and 37-GHz channels. We find that the root-mean-square direction difference between the Global Data Assimilation System winds and the closest WindSat wind ambiguity is less than 20° for above 7-m/s wind speed. The retrieval analysis supports the consistency of the Windrad05 GMF with the WindSat data.

**Index Terms**—Ocean surface wind, polarimetric radiometer, scatterometer, tropical cyclone.

## I. INTRODUCTION

THE ocean surface wind, generating the momentum flux affecting ocean circulation and mixing, is one of the key driving forces for the heat and moisture exchanges between the air and sea surfaces. Global ocean surface winds from the QuikSCAT scatterometer [1], operating since August 1999, have been routinely assimilated into the numerical weather prediction systems operated by the National Center for Environmental Prediction (NCEP) and European Center for Medium-Range Weather Forecasts (ECMWF).

As a potential alternate technique to active microwave radar, the passive microwave polarimetry [2] for ocean surface wind vector measurements has been investigated through several aircraft field campaigns [3]–[11]. Polarimetric passive microwave radiometry characterizes the microwave emissions by four Stokes parameters [2]. The vertically and horizontally polarized brightness temperatures ( $T_v$  and  $T_h$ ) represent the first two Stokes parameters. The third and fourth Stokes parameters,  $U$  and  $V$ , characterize the orientation and ellipticity of the polarized electromagnetic radiation. The past aircraft field campaigns have shown wind direction signals in all Stokes parameters for sea surface emissions. The directional signals in the spaceborne Special Sensor Microwave/Imager (SSM/I)

$T_v$  and  $T_h$  data extensively analyzed in [12] and [13] have compared very well with aircraft observations [13]. However, the strong response of  $T_v$  and  $T_h$  data to the atmospheric cloud liquid and water vapor does not allow robust wind direction estimates using the SSM/I-like dual-polarized satellite microwave radiometers. In contrast, the third and fourth Stokes parameters are less sensitive to cloud and water vapor as demonstrated in aircraft measurements [3]–[11] and are more suitable for the ocean wind direction measurements over a broader range of weather conditions.

The aircraft data show that the wind direction signals in  $U$  and  $V$  increase with wind speed and reach a few Kelvin for moderate and high winds (10–15-m/s wind speeds). An empirical geophysical model function (GMF) (Windrad99), relating the amplitude of  $U$  and  $V$  to ocean surface wind speed and direction, was derived from the Jet Propulsion Laboratory (JPL) aircraft Wind Radiometer (WINDRAD) measurements in the range of wind speed from 3–15 m/s [7].

To explore the polarimetric microwave signals for extreme high winds, the Hurricane Ocean Wind Experiment (HOWE) was conducted with a set of National Aeronautics and Space Administration (NASA) P-3 aircraft flights over Hurricane Erika in September 1997. The HOWE sensor suite included the Jet Propulsion Laboratory (JPL) Ku-band dual-polarized scatterometer (NUSCAT) [14] and JPL polarimetric 17-, 19-, and 37-GHz WINDRAD [5], [6]. In this paper, we will describe the characteristics of the WINDRAD/HOWE measurements to lend support to the satellite measurements for very high winds.

The spaceborne demonstration of passive polarimetry for large spatial coverage of ocean surface wind vectors is being performed by the WindSat multifrequency polarimetric radiometer [15], developed by the Naval Research Laboratory for the U.S. Navy and the National Polar-Orbiting Operational Environmental Satellite System (NPOESS) Integrated Program Office. The WindSat instrument was launched successfully on the Coriolis satellite mission in January 2003. We have analyzed six months of WindSat data to develop a GMF (Windrad05) for the third and fourth Stokes parameters. The WindSat GMF has been compared with the aircraft WINDRAD data to demonstrate consistency. We have also applied the GMF to wind retrieval from the WindSat data to validate the Windrad05 GMF and to assess the directional measurement performance of WindSat.

Section II describes the WINDRAD/HOWE data for extreme high winds (>20 m/s). Section III presents the signatures of WindSat polarimetric radiometer data. The wind direction harmonics of the Stokes parameters in the form of an empirical

Manuscript received January 30, 2005; revised July 26, 2005. The work was supported in part by the National Oceanic and Atmospheric Administration's National Polar-orbiting Operational Environmental Satellite System Integrated Program Office and in part by the National Aeronautics and Space Administration's Ocean Vector Wind Science Team.

The authors are with the Jet Propulsion Laboratory, California Institute of Technology, Pasadena, CA 91109 USA (e-mail: simon.yueh@jpl.nasa.gov).

Digital Object Identifier 10.1109/TGRS.2005.858416

geophysical model function are described in Section IV. The results of wind retrieval analysis are presented in Section V. We summarize the key findings in Section VI.

## II. AIRCRAFT HIGH WIND EXPERIMENT

In September 1997, JPL WINDRAD was deployed together with the NUSCAT on the NASA P-3 research aircraft. Two flights over Hurricane Erika were performed on September 10 and 11, 1997. Additional data were acquired over the National Data Buoy Center (NDBC) buoy 44004 during the transit flight from Bermuda to the Wallops Island on September 12, 1997. This flight campaign included circle flights for the WINDRAD passive microwave radiometers with antennas pointing toward the starboard at 75° elevation angle from the aircraft nadir axis. The circle flights were performed at three constant bank angles of 10°, 20°, and 30°, resulting in 65°, 55°, and 45° incidence angles for the WINDRAD, respectively.

Hurricane Erika reached its peak intensity of 110 knots on September 8, 1997 and retained this intensity for a period of 24 h. The hurricane passed about 300 nautical miles east of Bermuda on the 10th and turned toward the east–northeast on the 11th and 12th. The maximum wind speed estimated from the National Hurricane Center (NHC) best track analysis during the time of aircraft flights was about 80–90 knots (40–45 m/s) on the 10th and 65–70 knots (32–35 m/s) on the 11th. We had acquired data from one location on the 10th and three locations on the 11th to sample different wind conditions. There probably was rain in the area of NASA P-3 circle flights on September 10, 1997, while the atmosphere was nonprecipitating with stratus clouds over two areas and scattered clouds over one area of data acquisition on the 11th.

NUSCAT employed two axis gimbals to point a parabolic reflector antenna at selected incidence (0° to 65°) and azimuth angles. During the HOWE circle flights, we pointed the antenna toward the starboard at an elevation angle of 65° for right hand banks. Because the WINDRAD antenna boresight pointed at 75° in elevation, the NUSCAT incidence angle was lower than the WINDRAD incidence angle by 10°. This resulted in an offset between the WINDRAD and NUSCAT antenna footprints by about 2 km at 45° WINDRAD incidence angle and about 5 km at 65° WINDRAD incidence angle. The WINDRAD footprint size was about 4.5 km × 1.9 km at 65° incidence angle, while the NUSCAT footprint size was about 1 km × 0.6 km at 55° incidence angle. There was no overlap between the WINDRAD and NUSCAT footprints. However, the spatial offset did not seem to significantly decorrelate the directional signals in the coincident active and passive observations for nonprecipitating conditions.

During the HOWE deployment, the GPS dropsondes were launched from P-3 to perform *in situ* measurements. GPS dropsondes provided the measurements of wind speed and direction (horizontal winds), pressure, temperature, and humidity. The NUSCAT/HOWE data together with detailed descriptions of GPS dropsondes and acquired meteorological data were published in [14].

The atmospheric losses for the investigated locations (Table I) were estimated by using the technique described in [7], which compares the WINDRAD  $T_V$  and  $T_H$  measurements averaged

TABLE I  
SUMMARY OF SURFACE WIND AND ATMOSPHERIC CONDITIONS FOR JPL AIRCRAFT POLARIMETRIC RADIOMETER AND AIRCRAFT FLIGHTS IN 1997. ONE-WAY ATMOSPHERIC LOSSES IN DECIBELS AT 19 AND 37 GHz WERE ESTIMATED FROM THE RADIOMETER DATA AT 55° INCIDENCE ANGLE. THE VALUES FOR THE U.S. STANDARD ATMOSPHERE, EVALUATED USING THE MPM [19], WERE INCLUDED AS A REFERENCE

Date (month/day/year)	Start Time of the Flight Line in UT (hh:mm)	Target Location	Wind Speed (m/s)	Incidence Angle (degree)	Atmospheric Loss at 19.35 GHz	Atmospheric Loss at 37 GHz
9/10/97	21:48	1	29.5	65	2.92	3.87
9/10/97	22:03	1	29.5	55	2.15	2.86
9/10/97	22:12	1	27.7	45	1.75	2.32
9/11/97	16:39	2	28.5	65	0.91	1.22
9/11/97	16:59	2	22.2	55	0.67	0.90
9/11/97	17:08	2	22.2	45	0.54	0.72
9/11/97	17:59	3	28.5	65	1.36	1.76
9/11/97	18:17	3	26.5	55	0.99	1.27
9/11/97	18:26	3	34.4	45	0.79	1.03
9/11/97	19:16	4	32.7	65	1.25	1.89
9/11/97	19:35	4	35.2	55	0.92	1.38
9/11/97	19:45	4	35.2	45	0.75	1.13
9/12/97	17:18	NDBC 44004	9.4	65	0.85	1.09
9/12/97	17:13	NDBC 44004	9.4	55	0.63	0.70
9/12/97	17:10	NDBC 44004	9.4	45	0.53	0.58
		US Std. Atm.		65	0.48	0.73
		US Std. Atm.		55	0.35	0.54
		US Std. Atm.		45	0.28	0.44

over wind directions at 55° incidence angle with Wentz's SSM/I model values [17]. Location 1 had significant atmospheric attenuation, about 2 dB at 55° and 19.35 GHz. Location 2 was partly clear with broken scattered clouds and had a lower loss. Locations 3 and 4 had stratus cloud cover, but were probably nonprecipitating. If there was no rain at location 2, then the difference of the 19.35-GHz atmospheric losses between locations 1 and 2 suggests rain attenuation of about 1.5 dB at location 1, which would correspond to about 10 mm/h rain rate.

Figs. 1–3 illustrate the coincident active and passive microwave measurements at location 4 for Hurricane Erika. The data were plotted against the azimuth angle of antenna look direction with respect to the north for two consecutive circles. The normalized radar cross-sections for ( $\sigma_{\alpha\beta}$ ) are indicated in the upper two panels. The subscript  $\alpha$  stands for the receiving polarization, while the subscript  $\beta$  stands for the transmit polarization. The NUSCAT radar can transmit and receive vertical polarization (V) or horizontal polarization (H).

The radar data acquired at the 55° incidence angle along with the radiometer data acquired at 65° incidence angle are illustrated in Fig. 1. The peaks of  $\sigma_{VV}$  and  $\sigma_{HH}$  agree well with the wind direction reported by the dropsonde. The cross-polarized response  $\sigma_{HV}$  has similar characteristics to  $\sigma_{VV}$  and  $\sigma_{HH}$ . At this location the brightness temperature  $T_v$  was quite high (>240 K), indicative of high atmospheric loss. However, the differences between  $T_v$  and  $T_h$  remain large, about 20–40 K at K-band (19 GHz). The substantial polarization difference does not suggest the presence of heavy precipitation. Although  $T_v$  and  $T_h$  data share similar azimuth direction features, they are uncorrelated with the wind direction. It is likely that the cloud cover or humidity was nonuniform during flight circles, and hence overwhelmed the directional variations of  $T_v$  and  $T_h$  expected for clear sky conditions. Unlike  $T_v$  and  $T_h$ , the wind direction response of the third and fourth Stokes parameters is

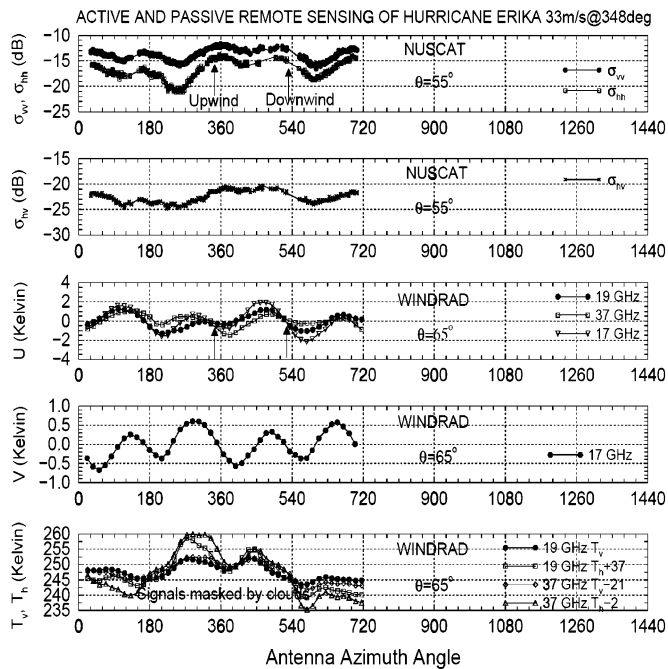


Fig. 1. Coincident Ku-band ocean backscatter and polarimetric brightness temperatures of sea surfaces versus antenna azimuth look angle. The upper two panels plot the NUSCAT  $\sigma_{VV}$ ,  $\sigma_{HH}$ , and  $\sigma_{HV}$  backscatter data at  $55^\circ$  incidence angle. The bottom three panels plot the Stokes parameters acquired at  $65^\circ$  incidence. The data were acquired on September 11, 1996 with NASA P-3 flights over Hurricane Erika. The dropsonde wind was 32.7 m/s at  $348^\circ$  from the north.

apparent. The magnitude of azimuth modulations is about 4 K in  $U$  and 1 K in  $V$  at 17 GHz. The 37-GHz data have smaller amplitudes for  $U$ , likely due to larger atmospheric attenuation. The directional modulations of  $U$  and  $V$  resemble the sinusoidal function, orthogonal to the cosine dependence of radar  $\sigma_{VV}$  and  $\sigma_{HH}$ .

Fig. 2 illustrates the data at lower incidence angles,  $45^\circ$  for radar and  $55^\circ$  for radiometer. The radar  $\sigma_{VV}$  and  $\sigma_{HH}$  data indicated clear wind direction dependence. The cross-polarized echoes had similar features, but had a corrupted directional response over the first part of the second circle. The radiometer  $U$  and  $V$  data indicated sinusoidal response with the direction of zero crossings lining up very well with the radar data. The amplitudes of  $U$  and  $V$  are similar to those at  $65^\circ$  incidence angle.

Reducing the aircraft bank angle (or incidence angle) by another  $10^\circ$  resulted in the data illustrated in Fig. 3. The radar data at  $35^\circ$  incidence angle showed clear correlation with wind direction for all polarization channels, although  $\sigma_{HV}$  data indicated noisier response near the azimuth angle of  $720^\circ$ . Similar to the data at higher incidence angles, the radiometer  $T_v$  and  $T_h$  data showed clear influence of clouds, while  $U$  and  $V$  data have good correlations with the wind direction. The amplitude of  $U$  is about 4 Kelvin, similar to the data at  $55^\circ$  and  $65^\circ$  incidence angles. The most dramatic change is the amplitude of  $V$  reducing to about 0.5 K peak-to-peak from 1 K at  $55^\circ$  and  $65^\circ$  incidence angles.

We have examined the data from locations 1, 2, and 3. The characteristics of these data are essentially the same as those illustrated in Figs. 1–3. The only major difference was a lesser cloud coverage over location 2, where there were broken scat-

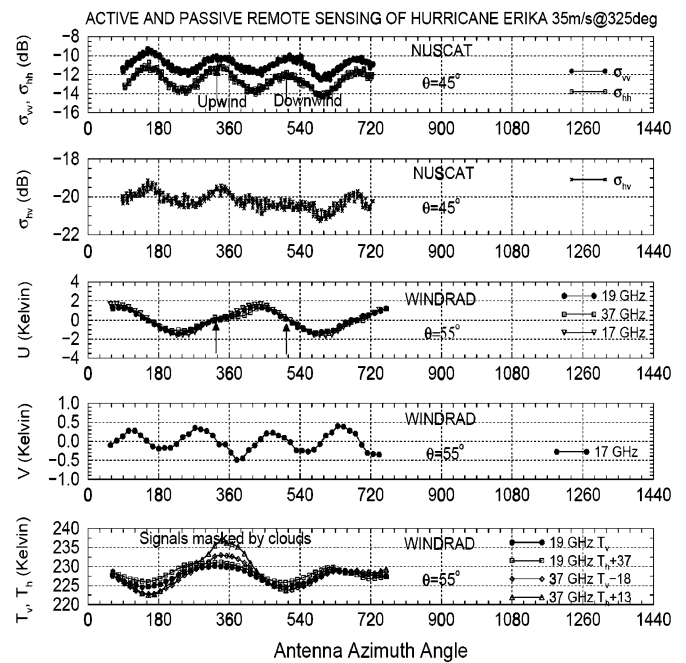


Fig. 2. Coincident Ku-band ocean backscatter and polarimetric brightness temperatures of sea surfaces versus antenna azimuth look angle. The upper two panels plot the NUSCAT  $\sigma_{VV}$ ,  $\sigma_{HH}$ , and  $\sigma_{HV}$  backscatter at  $45^\circ$  incidence. The bottom three panels plot the Stokes parameters acquired at  $55^\circ$  incidence angle. The data were acquired on September 11, 1996 with NASA P-3 flights over Hurricane Erika. The dropsonde wind was 35.2 m/s at  $325^\circ$  from the north.

tered clouds in some regions, but appeared to be clear for many areas. Consequently, the wind direction dependence was observable in the  $T_v$  and  $T_h$  data from location 2 with their signatures similar to the data acquired for moderate winds (5–12 m/s) during 1993–1996 flight campaigns.

The key features of the coincident radar and radiometer data acquired from flights in 1997 can be summarized as follows.

- There were wind direction signals in the third and fourth Stokes parameters of radiometer data for up to 35-m/s winds, even under the presence of cloud cover. Radar and radiometer data suggest consistent wind directions for clear and cloudy skies for 10–35-m/s wind speed.
- The radar data showed decreasing directional modulation from 5 to 2 dB for wind speed increasing from 10 to 35 m/s, while the peak-to-peak modulation of the third Stokes parameter  $U$  remained essentially unchanged.
- The radar data had small upwind and downwind asymmetry with a dominant second cosine harmonics for high winds, while the passive third Stokes parameter data had a strong upwind and downwind asymmetry with significant first harmonics.

### III. WINDSAT POLARIMETRIC MICROWAVE SIGNATURES

The WindSat polarimetric multifrequency radiometer consists of five frequency channels, 6.8, 10.7, 18.7, 23.8, and 37 GHz, respectively, at the incidence angles of  $53.5^\circ$ ,  $49.9^\circ$ ,  $55.3^\circ$ ,  $53.0^\circ$ , and  $53.0^\circ$ . The 10-, 18-, and 37-GHz channels have fully polarimetric capability for  $T_v$ ,  $T_h$ ,  $U$ , and  $V$  measurements. The 6- and 23-GHz channels are dual-polarized

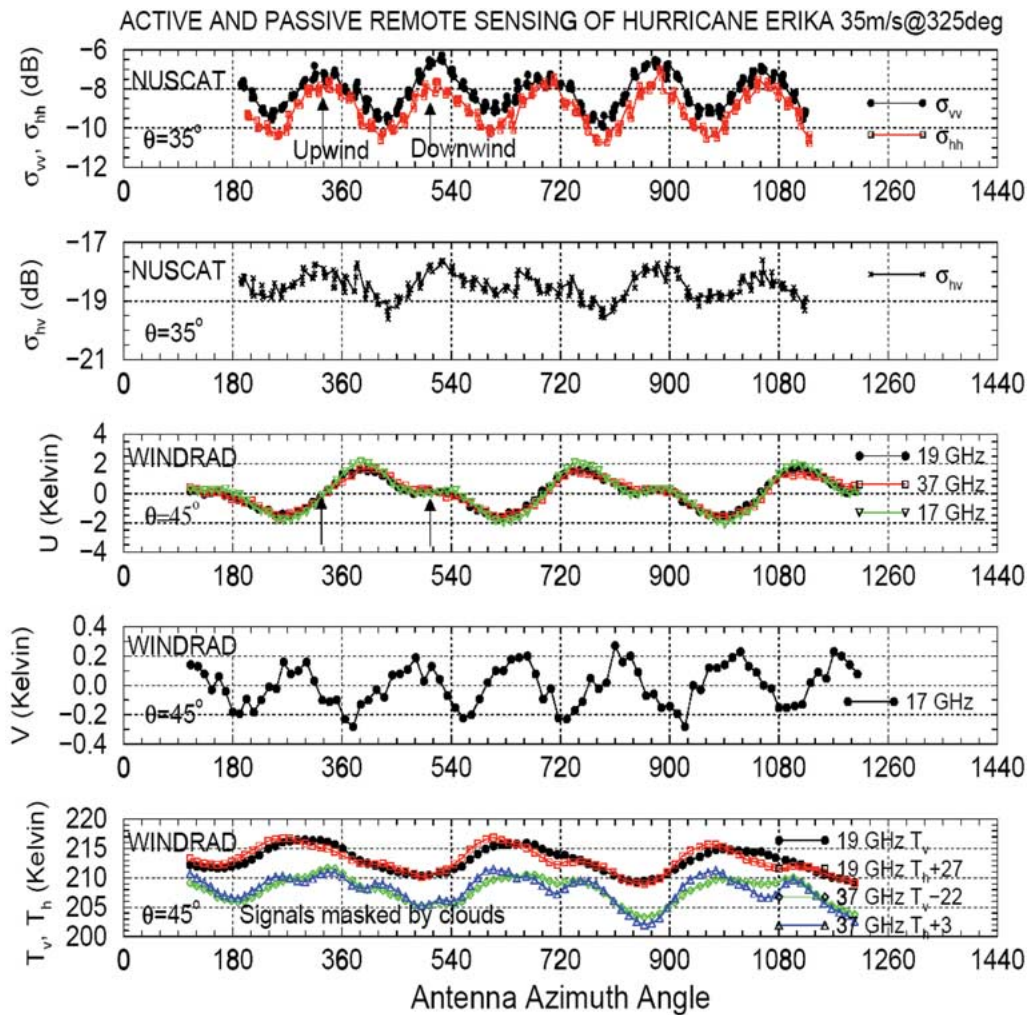


Fig. 3. Coincident Ku-band ocean backscatter and polarimetric brightness temperatures of sea surfaces versus antenna azimuth look angle. The upper two panels plot the NUSCAT  $\sigma_{VV}$ ,  $\sigma_{HH}$ , and  $\sigma_{HV}$  backscatter at  $35^\circ$  incidence. The bottom three panels plot the Stokes parameters acquired at  $45^\circ$  incidence. The data were acquired on September 11, 1996 with NASA P-3 flights over Hurricane Erika. The dropsonde wind was 35.2 m/s at  $325^\circ$  from the north.

for  $T_v$  and  $T_h$  observations only. The integrated field of view (IFOV) is  $40 \text{ km} \times 60 \text{ km}$ ,  $25 \text{ km} \times 38 \text{ km}$ ,  $16 \text{ km} \times 27 \text{ km}$ ,  $12 \text{ km} \times 20 \text{ km}$ , and  $8 \text{ km} \times 13 \text{ km}$ , respectively, for 6-, 10-, 18-, 23-, and 37-GHz channels. Because the wind directional dependence of  $T_v$  and  $T_h$  has been extensively investigated in [13], we focus our investigation on the characteristics of  $U$  and  $V$  data.

We have obtained six months of WindSat brightness temperature data from September 2003 through February 2004. In addition, the WindSat project also provided the collocated environmental analysis from the NCEP Global Data Assimilation System (GDAS). The GDAS analysis was produced on  $1^\circ \times 1^\circ$  grids at 00Z, 06Z, 12Z, and 18Z. The matchup algorithm, using the closest GDAS analysis in time (within  $\pm 3$  h), selects four GDAS points surrounding each WINDSAT footprint location, and spatially interpolates the GDAS geophysical parameters to the WINDSAT antenna footprint location. The WindSat data for the matchup were binned on the IFOV resolution ( $40 \text{ km} \times 60 \text{ km}$ ) of the 6-GHz channel, about a factor of two higher resolution than the GDAS grids. The GDAS analysis consists of ocean surface wind speed, wind direction, water

temperature, atmospheric water vapor, and liquid water. For each GDAS and WINDSAT data matchup, we estimated the atmospheric transmittance ( $\tau$ ) at each frequency using the technique described in [7] to remove the atmospheric attenuation effects on  $U$  and  $V$  data. This technique compares the WINDSAT  $T_v$  and  $T_h$  data against the surface emissivity predicted from the Advanced Microwave Scanning Radiometer (AMSR) model function [18] using the GDAS wind speed and water temperature as the input. After the estimate of  $\tau$  is achieved, the  $U$  (or  $V$ ) data are corrected for the atmospheric attenuation by

$$U = U' / \tau^2.$$

Here  $U'$  signifies the WindSat measurements on the top of atmosphere.

The corrected  $U$  and  $V$  data are binned as a function of the GDAS wind speed and relative wind direction at 1-m/s and  $10^\circ$  step. The relative wind direction is the difference between the GDAS wind direction and the azimuth angle of the WindSat look direction. Fig. 4 plots the average and standard deviation

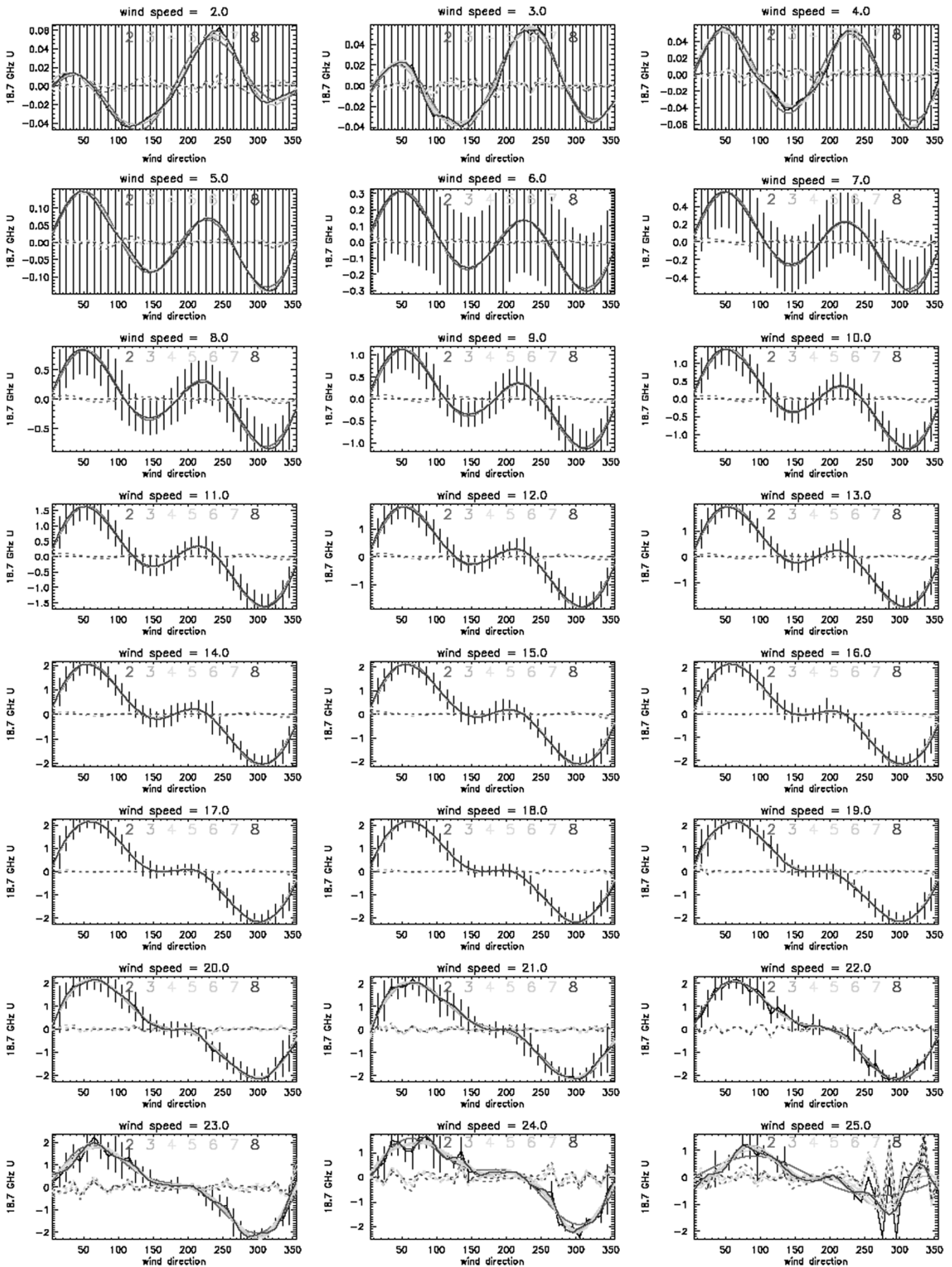


Fig. 4. WindSat 18-GHz  $U$  data binned as a function the NCEP GDAS wind direction from 1–25-m/s wind speed.

of the 18-GHz  $U$  data in each bin as a function of the wind direction from 1–25-m/s wind speeds. There are sinusoidal signals in all the panels with the peak of the sinusoids as low as 0.05 K at lower than 5-m/s wind speed and as large as 2 K in the range of 15–20-m/s wind speed. The amplitude of signals is clearly larger than the standard deviations, about 0.5 K for 5–15-m/s wind speeds, suggesting the statistical significance of the observed sinusoidal signals. For wind speeds above 23 m/s, the number of GDAS high-wind analysis reduces significantly, resulting in degraded sinusoidal features. At 24- and 25-m/s wind speeds, a lack of samples in several wind direction bins makes this WindSat and GDAS matchup analysis less reliable.

In each panel, we include the curves of the truncated sine series with coefficients selected to fit the data using the least square error criterion. The curves for sine series of two, three, and up to eight terms are hardly separable. We find that the first two terms of the sine series fit the data quite well. It is clear that the first harmonics dominate the sine series for wind speed greater than 5 m/s. The amplitude of the third and fourth terms of the sine series are near zero for low winds and increases to about 0.1 K for moderate and high winds. The set of curves near the horizontal axis corresponds to the difference between the averaged WindSat data and the sine series in each bin. The difference is mostly less than 0.1 K for less than 20-m/s wind speeds, but frequently exceeds 0.3 K for higher than 23-m/s wind speeds. We therefore conclude that keeping only the first two terms of the sine series provides accurate representation of the wind direction features in WindSat data.

The  $V$  data are illustrated in Fig. 5. Like the  $U$  data, there are clear directional signals in all the panels except for 24- and 25-m/s winds. The standard deviation is quite small, less than 0.2 K for most cases, indicating the statistical significance of observed directional signals. The directional characteristics of  $V$  data are dominated by the second harmonics, unlike the  $U$  data with a dominant first harmonics. The features of WindSat  $U$  and  $V$  data agree very well with the aircraft observations reported in [5]–[10].

We have performed similar analysis on the  $U$  and  $V$  data at 10 and 37 GHz. The directional features in the 10-GHz  $U$  and  $V$  and 37-GHz  $U$  data are as robust and are very similar to those at 18 GHz. The exception is the 37-GHz  $V$  data, which have much smaller directional response than the lower frequency channels.

#### IV. WIND DIRECTION HARMONICS

This section explores the amplitude of wind direction harmonics in polarimetric brightness temperatures through the comparison of WindSat data with existing model functions and aircraft data. The objective is to achieve an empirical GMF to enable wind direction retrievals over a wide range of wind speeds for WindSat.

For reflection symmetric surfaces it has been shown from Maxwell's equations [16] that  $T_v$  and  $T_h$  are even functions of azimuth angle  $\phi$  and  $U$  and  $V$  are odd functions with  $\phi = 0$  representing the symmetry plane. These general symmetry properties have been demonstrated in the aircraft, SSM/I and WindSat measurements for wind-generated sea surfaces, which are expected to be statistically reflection symmetric with respect to

the wind direction  $\phi_W$ . This suggests that the Stokes parameters can be expanded by cosine or sine series of the relative azimuth angles  $\phi$

$$\begin{aligned} T_V &= T_{V0} + T_{V1} \cos \phi + T_{V2} \cos 2\phi \\ T_H &= T_{H0} + T_{H1} \cos \phi + T_{H2} \cos 2\phi \\ U &= U_1 \sin \phi + U_2 \sin 2\phi \\ V &= V_1 \sin \phi + V_2 \sin 2\phi. \end{aligned}$$

Here,  $\phi = \phi_W - \phi_R$  with  $\phi_W$  and  $\phi_R$  representing the azimuth angle of wind and radiometer look directions, respectively. The coefficients of the first harmonics account for upwind and downwind asymmetric surface features, while those of the second harmonics account for the upwind and crosswind asymmetry.

Note that the definition of WindSat  $U$  and  $V$  data is off by a minus sign from the aircraft WindRad data. We have inverted the sign of the WindSat  $U$  and  $V$  coefficients illustrated in Figs. 6–8 for comparison with aircraft observations [5]–[7].

The lower four panels of Fig. 6 compare the K-band WindSat harmonics coefficients for  $U$  and  $V$  with the aircraft Windrad radiometer data and the empirical Windrad GMF. The absolute magnitude of  $U_1$  is small for lower than 5-m/s winds, increases rapidly with increasing wind speed from low to moderate winds and levels off above 15-m/s wind speed. In comparison  $V_1$  is very small and has no distinctive wind speed dependence. The amplitude of  $U_2$  and  $V_2$  increases from light to 12-m/s wind speed and decreases in amplitude beyond 15–20 m/s. This feature is consistent with the wind speed response of the second harmonics of Ku-band spaceborne radar data, which also have an initial increase followed by a decrease with increasing wind speed [20]. The characteristics of the WindSat  $U$  and  $V$  data agree very well with the aircraft WINDRAD data.

The Ka-band (37 GHz)  $U$  and  $V$  harmonics data are illustrated in Fig. 7. The WindSat  $U_1$  data agree well with the aircraft data. The response of  $U_2$  to wind speed also agrees well although the WindSat  $U_2$  data are stronger than the aircraft data at near 15-m/s wind speed, probably due to limited sampling statistics of the aircraft measurements. The characteristics of the Ka-band data are very similar to these of K-band data.

The exception is the significantly smaller  $V_2$  at Ka-band than at K-band. This is opposite to the relative magnitude of  $U_2$  at these two frequency bands with the WindSat data indicating slightly stronger  $U_2$  data at Ka-band. If the Bragg scattering mechanism in the two-scale scattering model is the key driver for both  $U$  and  $V$  data, then  $V_2$  data at Ka-band should not be so much weaker [11]. The WindSat Ka-band  $V$  data, if accurate, provides experimental evidence indicating deficiency in the two-scale ocean scattering model for ocean surfaces.

The upper four panels of Figs. 6 and 7 compare the  $T_v$  and  $T_h$  harmonics data from the aircraft measurements and three empirical models, including the empirical model (MW2002) produced by Meissner and Wentz [11]. The empirical model function, Windrad99, was an empirical fit of the aircraft Windrad data acquired before 1997 [7], and the empirical model Windrad05 was retuned from the Windrad99 model to match the MW2002 model and to produce better wind retrievals for WindSat data processing for high winds. The revision of the

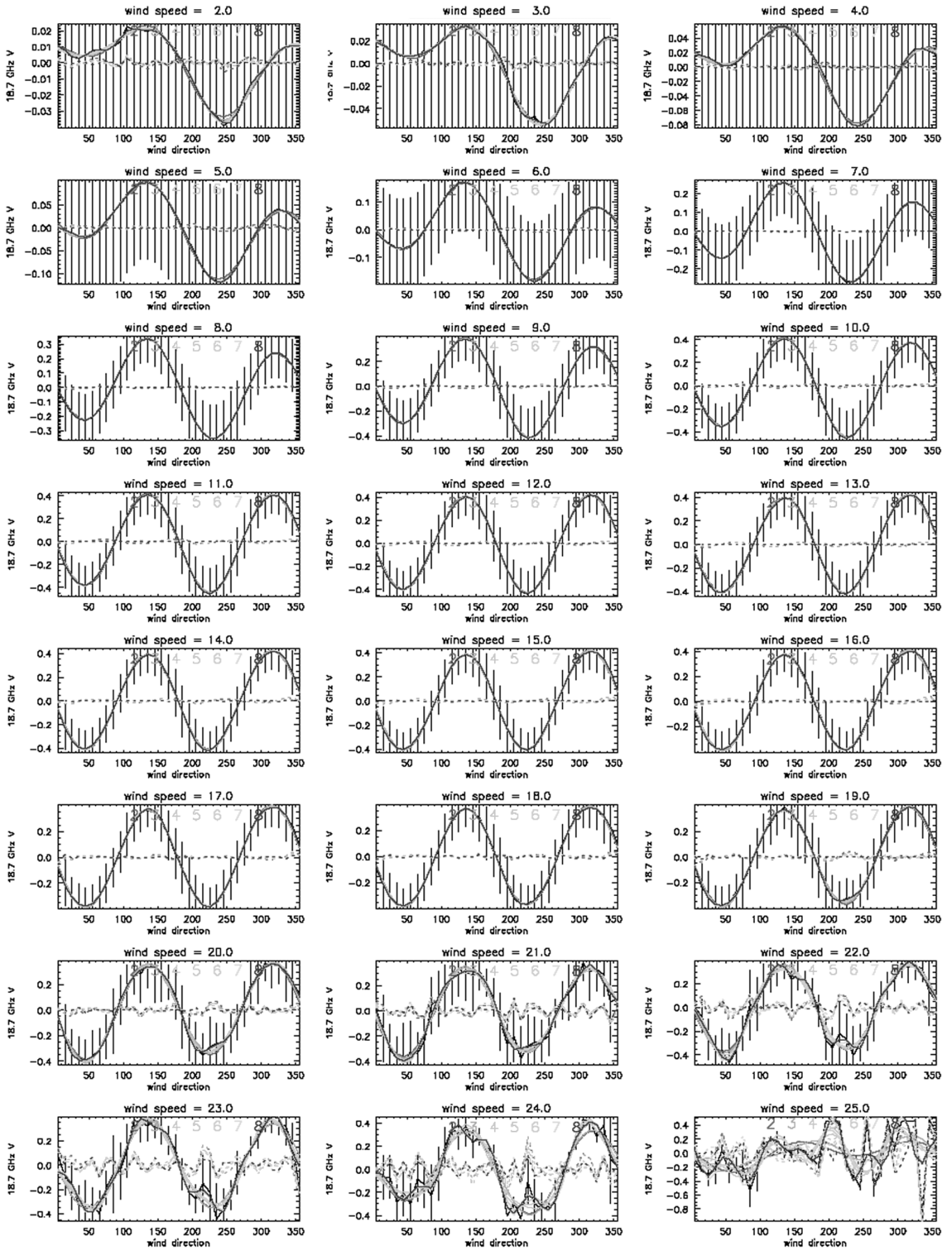


Fig. 5. WindSat 18-GHz V data binned as a function the NCEP GDAS wind direction from 1–25-m/s wind speed.

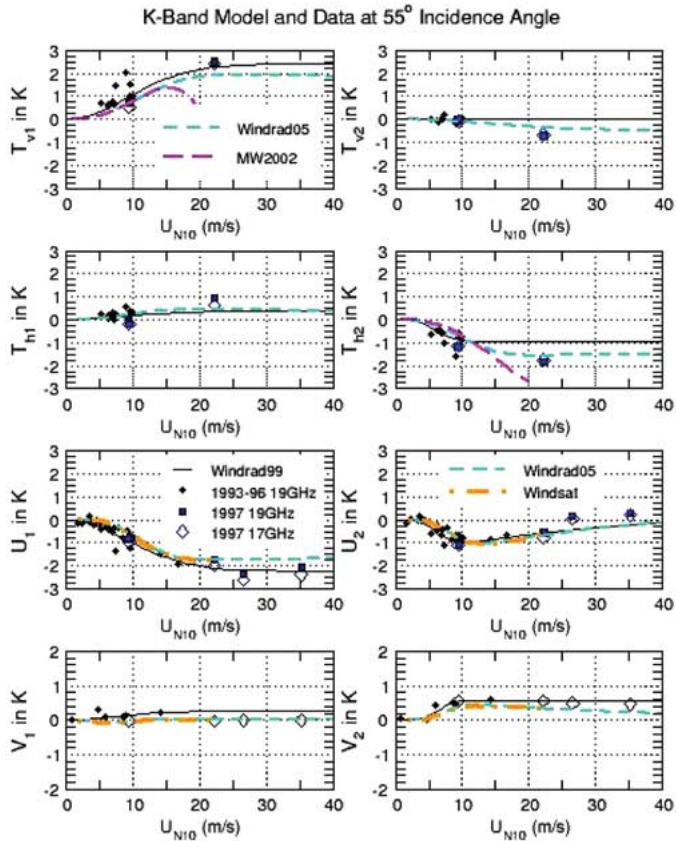


Fig. 6. Directional harmonic coefficients of K-band brightness temperatures versus wind speed at a nominal incidence angle of  $55^\circ$ . The scattered diamonds and rectangles are the JPL WINDRAD data acquired from flight campaigns during 1993–1997. The dotted–dashed lines correspond to the harmonics coefficients derived from the WindSat data. Thin solid curves correspond to the empirical Windrad99 model function [7], while the short-dashed lines correspond to the empirical Windrad05 model tabulated in Table II. The long-dashed lines illustrated in the panels for  $T_{V1}$  and  $T_{H2}$  are the empirical model derived from the MW2002 model by Meissner and Wentz [13].

MW2002 model for high winds will be further discussed in the next section.

The aircraft data and the MW2002 model both show that  $T_{h1}$  and  $T_{v2}$  data are small and have no distinctive wind speed dependence. The amplitude of  $T_{v1}$  appears to be similar to  $U_1$  at less than 10 m/s, except with a sign difference. Without sufficient data for  $T_{v1}$  at greater than 15 m/s, it is unclear if  $T_{v1}$  also saturates for high winds (greater than 20 m/s).

Fig. 8 compares the WindSat data and the empirical MW2002 and Windrad05 models at X-band. Note that the Windrad05 model at X-band was essentially tuned from the WindSat data for  $U$  and  $V$  and from the MW2002 model for  $T_v$  and  $T_h$ . The changes made to the MW2002 model are to saturate  $T_{v1}$  and  $T_{h2}$  for high winds. It is shown that the behavior of  $U$  and  $V$  coefficients versus wind speed is very similar to that at K-band, except with a smaller magnitude. One interesting difference from the 18- and 37-GHz channels is the wind speed for which the peak  $U_2$  amplitude is achieved. The absolute magnitude of  $U_2$  reaches maximum at near 15 m/s at X-band, but peaks near 11–12 m/s at K-band and Ka-band. This suggests that the upwind and crosswind asymmetry of sea surfaces increases less rapidly for light to moderate winds at lower microwave frequencies.

The harmonics coefficients derived from the K-band Windrad data for  $45^\circ$  and  $65^\circ$  incidence angles are illustrated in

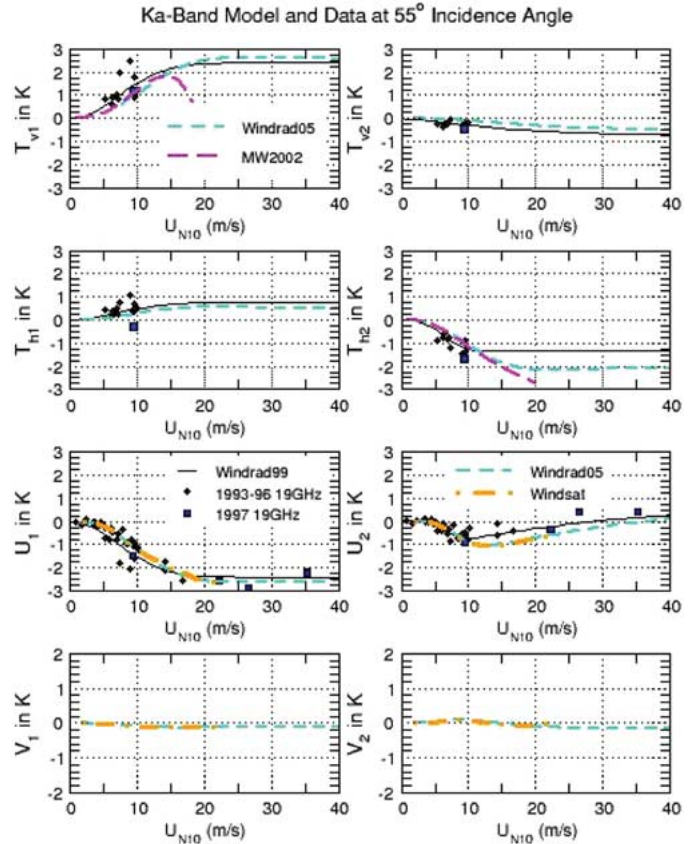


Fig. 7. Same as Fig. 6 except for Ka-band.

Figs. 9 and 10. The first harmonics coefficients at  $45^\circ$  incidence angle have very similar wind speed response to those at  $55^\circ$  incidence angle, but have slightly smaller amplitudes. In contrast, the data at  $65^\circ$  incidence angle illustrated in Fig. 10 show larger  $T_{v1}$  and  $U_1$  than at  $55^\circ$  incidence angle. This is consistent with the expectation that the effects of the upwind and downwind asymmetry of ocean surfaces, in the form of skewness in surface slopes, asymmetric distribution of capillary waves, breaking waves, and sea foam on the long waves, are more pronounced at higher incidence angles, similar to what is indicated in the Ku-band ocean backscatter.

Regarding the upwind and crosswind asymmetry, the characteristics of  $T_{h2}$  and  $V_2$  data at  $45^\circ$  and  $65^\circ$  incidence angles are similar to those at  $55^\circ$  incidence angle. However, the wind speed response of  $T_{v2}$  and  $U_2$  changes significantly over incidence angles.  $T_{v2}$  is positive at  $45^\circ$  incidence angle for at least up to 20-m/s wind speeds (Fig. 9), slightly negative at  $55^\circ$  incidence angle (Fig. 6), and clearly negative at  $65^\circ$  incidence angle (Fig. 10). Examining the data acquired at 22 m/s shows that  $T_{v2}$  changes from positive to negative as the incidence angle increases from  $45^\circ$  to  $55^\circ$ . The phase transition of  $U_2$  at high wind speeds is even more pronounced than that of  $T_{v2}$  as shown in Figs. 6, 9, and 10. At 35-m/s wind speed,  $U_2$  is negative at  $45^\circ$  incidence angle (Fig. 9), but becomes positive at  $65^\circ$  incidence angle (Fig. 10). This kind of phase transition versus incidence angle appears to be consistent with the theoretical signature of Bragg scattering by short-gravity and capillary waves [11].

The characteristics of K-band (17 and 19 GHz) and Ka-band (37 GHz) data are very similar in terms of wind speed depen-

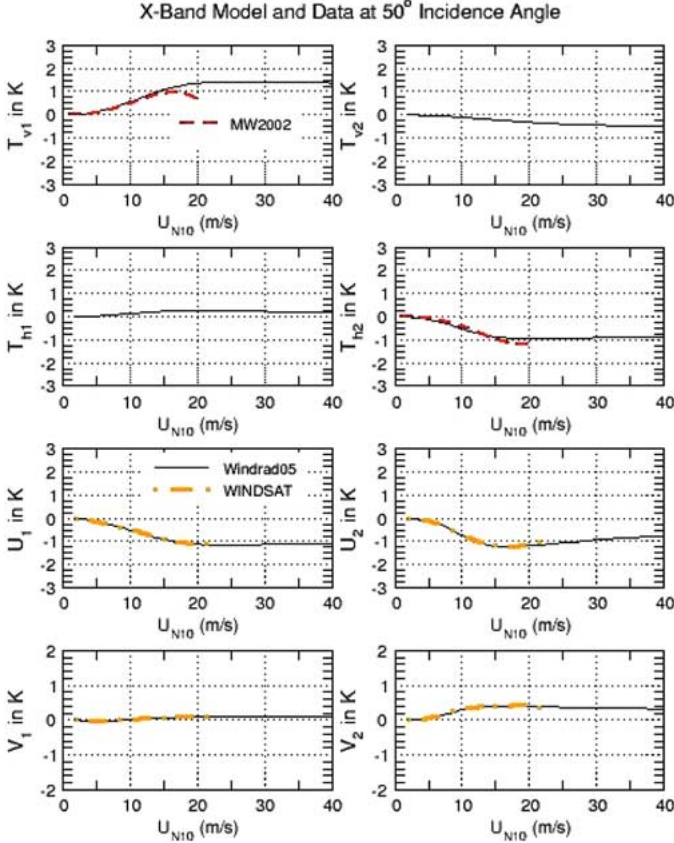


Fig. 8. Directional harmonic coefficients of WindSat X-band brightness temperatures (dotted-dashed curves) versus wind speed at a nominal incidence angle of  $50^\circ$ . Thin solid lines correspond to the empirical model with coefficients tabulated in Table IV. The dashed lines illustrated in the panels for  $T_{V1}$  and  $T_{H2}$  are the empirical model derived from the MW2002 model [13].

dence for each incidence angle and polarization (Figs. 1–3). Because of the similarity at these two frequency bands, only the 37-GHz harmonic coefficients at  $55^\circ$  incidence angle are compared in Fig. 7 with the MW2002 model function [13].

As suggested by the data illustrated in Figs. 6–10, indicating a rapid increase of directional signals at low wind speeds and a saturation or phase change at high wind speeds, the following exponential function was selected to fit the Fourier coefficients as a function of the neutral wind speed at 10-m elevation ( $U_{N10}$ )

$$f(U_{N10}) = c_1 \{1 - \exp[-(U_{N10}/a_1)^{\alpha_1}]\} + c_2 \{1 - \exp[-(U_{N10}/a_2)^{\alpha_2}]\}. \quad (1)$$

The second term in the above equation was included primarily to model the phase transition of  $T_{v2}$  and  $U_2$  over incidence angles.

Tables II–IV summarize the coefficients for the Windrad05 model. The Windrad05 model is an update of the Windrad99 model [7] using the Windrad data acquired for high winds, the WindSat data and the MW2002 model. In general, the empirical curves fit the data very well. The empirical fit for  $U_1$  and  $U_2$  data suggests that the harmonics coefficients grow with an exponent ( $\alpha_1$ ) of about 2.5 at low wind speeds.

Note that the MW2002 model was derived using the SSM/I data for up to 14-m/s wind speed. The illustration of the MW2002 model for  $T_{v1}$  and  $T_{h2}$  was an extrapolation for

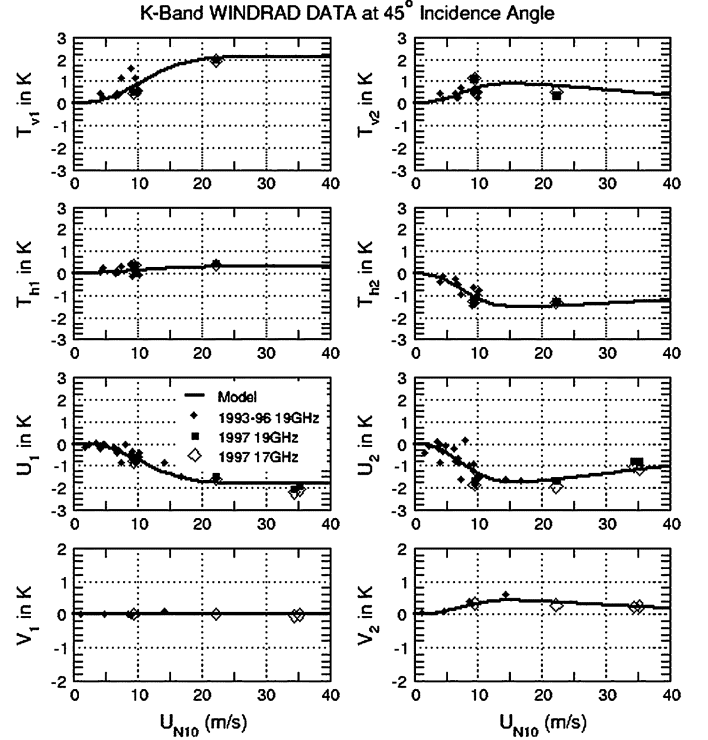


Fig. 9. Directional harmonic coefficients of K-band brightness temperatures versus wind speed at a nominal incidence angle of  $45^\circ$ . The scattered diamonds and rectangles are the JPL WINDRAD data acquired from flight campaigns during 1993–1997. Thick solid lines correspond to the empirical model with coefficients tabulated in Table II.

higher wind speeds. We find from the retrieval analysis described in the next section that the  $T_{v1}$  should continue to increase and saturate, while  $T_{h2}$  should slowly level off for wind speed beyond 15 m/s. This adjustment was made in the Windrad05 model using the Windrad data at 22-m/s wind speed and the MW2002 model to refit the empirical model function described in (1).

## V. WIND RETRIEVAL TESTING

We apply the empirical geophysical model function described in the above section to the wind speed and direction retrievals from the WindSat data. Through this process, we demonstrate the consistency of the model function with the WindSat data.

For the WindSat retrieval, we assume the following model to account for the effects of atmospheric attenuation and radiation

$$T_{Va} = T_{V\text{iso}} + \tau^2 \Delta T_V(W, \phi) \quad (2a)$$

$$T_{Ha} = T_{H\text{iso}} + \tau^2 \Delta T_H(W, \phi) \quad (2b)$$

$$U_a = \tau^2 U(W, \phi) \quad (2c)$$

$$V_a = \tau^2 V(W, \phi). \quad (2d)$$

The quantities on the left-hand side of the equations are the polarimetric brightness temperatures at the top of atmosphere.  $T_{V\text{iso}}$  and  $T_{H\text{iso}}$  are the vertically and horizontally polarized brightness temperatures of sea surfaces without wind direction effects, and are functions of wind speed, integrated atmospheric water vapor (WV), integrated atmospheric liquid water (LW),

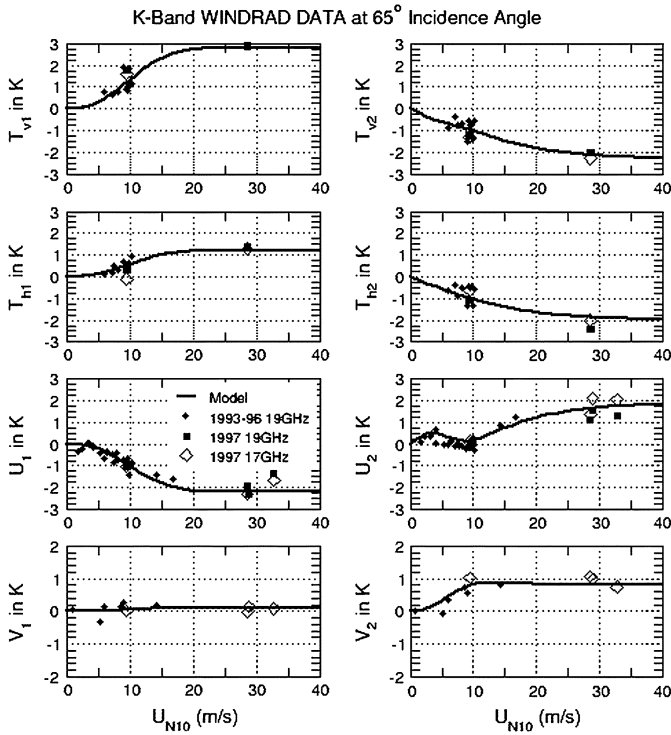


Fig. 10. Directional harmonic coefficients of K-band brightness temperatures versus wind speed at a nominal incidence angle of 65°. The scattered diamonds and rectangles are the JPL WINDRAD data acquired from flight campaigns during 1993–2000. Thick solid lines correspond to the empirical model with coefficients tabulated in Table III.

TABLE II  
WIND DIRECTION MODELING COEFFICIENTS FOR POLARIMETRIC  
BRIGHTNESS TEMPERATURES AT 19 GHz

Parameter	Incidence Angle	C <sub>1</sub>	a <sub>1</sub>	α <sub>1</sub>	c <sub>2</sub>	a <sub>2</sub>	α <sub>2</sub>
T <sub>v1</sub>	45	2.1	13	2.5	0	-	-
T <sub>h1</sub>	45	0.3	13	2.5	0	-	-
U <sub>1</sub>	45	-1.8	13	2.5	0	-	-
V <sub>1</sub>	45	0	-	-	0	-	-
T <sub>v2</sub>	45	1	9	2.5	-1	40	2.5
T <sub>h2</sub>	45	-1.6	9	2.5	0.6	40	2.5
U <sub>2</sub>	45	-1.9	9	2.5	1.4	40	2.5
V <sub>2</sub>	45	0.5	9	2.5	-0.5	40	2.5
T <sub>v1</sub>	55	2	13.5	2.5	-0.2	40	2.5
T <sub>h1</sub>	55	0.5	12.5	2.5	-0.2	40	2.5
U <sub>1</sub>	55	-1.8	12.5	3.4	0.2	40	2.5
V <sub>1</sub>	55	-0.2	6	2.5	0.2	10	3
T <sub>v2</sub>	55	-0.5	20	2	0	-	-
T <sub>h2</sub>	55	-1.8	12	2.5	0.3	20	2.5
U <sub>2</sub>	55	-1.35	9	3.3	1.4	28	2
V <sub>2</sub>	55	0.5	8.2	3.5	-0.35	28	2
T <sub>v1</sub>	65	2.8	12	2.5	0	-	-
T <sub>h1</sub>	65	1.2	12	2.5	0	-	-
U <sub>1</sub>	65	-2.2	12	2.5	0	-	-
V <sub>1</sub>	65	0.1	12	2.5	0	-	-
T <sub>v2</sub>	65	0.7	7	2.5	-3	12	1.2
T <sub>h2</sub>	65	0.2	7	2.5	-2.2	12	1.2
U <sub>2</sub>	65	-2.5	7	2.5	4.4	12	1.2
V <sub>2</sub>	65	1	7	2.5	-0.2	12	1.2

and sea surface temperature. The atmospheric attenuation is denoted by  $\tau$ , which is a function of WV and LW.  $T_{V_{iso}}$ ,  $T_{H_{iso}}$ , and  $\tau$  are modeled by Wentz's AMSR ocean algorithm [18]. The atmospheric attenuation and radiation reflected by the ocean surfaces have effectively two-way attenuation impact on the wind direction signals.

TABLE III  
WIND DIRECTION MODELING COEFFICIENTS FOR POLARIMETRIC  
BRIGHTNESS TEMPERATURES AT 37 GHz

Parameter	Incidence Angle	C <sub>1</sub>	a <sub>1</sub>	α <sub>1</sub>	c <sub>2</sub>	a <sub>2</sub>	α <sub>2</sub>
T <sub>v1</sub>	45	0.5	13	2.5	0	-	-
T <sub>h1</sub>	45	0.7	13	2.5	0	-	-
U <sub>1</sub>	45	-2.0	13	2.5	0	-	-
T <sub>v2</sub>	45	0.5	8	2.5	-1.2	40	2
T <sub>h2</sub>	45	-1.6	8	2.5	0.6	40	2
U <sub>2</sub>	45	-1.7	8	2.5	1.4	40	2
T <sub>v1</sub>	55	2.7	13.5	2.5	-0.2	40	2.5
T <sub>h1</sub>	55	0.6	12.5	2.5	-0.2	40	2.5
U <sub>1</sub>	55	-2.7	12.5	2.5	0.2	40	2.5
V <sub>1</sub>	55	-0.15	10	2.5	0.05	25	3
T <sub>v2</sub>	55	-0.5	20	2	0	-	-
T <sub>h2</sub>	55	-2.4	12	2.5	0.3	20	2.5
U <sub>2</sub>	55	-1.4	9	3.5	1.7	28	2
V <sub>2</sub>	55	0.2	7	3.5	-0.35	15	2.5
T <sub>v1</sub>	65	3.3	12	2.5	0	-	-
T <sub>h1</sub>	65	2.6	12	2.5	0	-	-
U <sub>1</sub>	65	-3	12	2.5	0	-	-
T <sub>v2</sub>	65	0.7	6	2.5	-3.4	12	1.2
T <sub>h2</sub>	65	0.2	6	2.5	-2.2	12	1.2
U <sub>2</sub>	65	-2.3	6	2.5	4.5	12	1.2

TABLE IV  
WIND DIRECTION MODELING COEFFICIENTS FOR POLARIMETRIC  
BRIGHTNESS TEMPERATURES AT 10.7 GHz

Parameter	Incidence Angle	C <sub>1</sub>	a <sub>1</sub>	α <sub>1</sub>	c <sub>2</sub>	a <sub>2</sub>	α <sub>2</sub>
T <sub>v1</sub>	50	1.5	13.5	2.5	-0.2	40	2.5
T <sub>h1</sub>	50	0.3	12.5	2.5	-0.2	40	2.5
U <sub>1</sub>	50	-1.2	12.5	2.5	-0.2	40	2.5
V <sub>1</sub>	50	-0.12	6	2.5	0.2	10	2.5
T <sub>v2</sub>	50	-0.5	20	2	0	-	-
T <sub>h2</sub>	50	-1.2	12	2.5	0.3	20	2.5
U <sub>2</sub>	50	-1.55	11	3	0.9	28	2
V <sub>2</sub>	50	0.5	9.5	3	-0.2	15	2.5

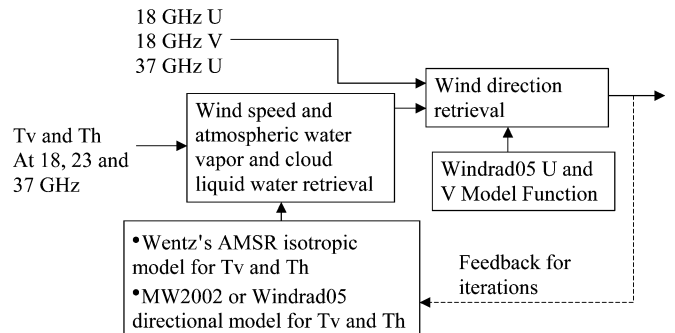


Fig. 11. Wind retrieval algorithm using an iterative approach to estimate wind speed, wind direction, water vapor, and cloud liquid water.

We employ an iterative approach, illustrated in Fig. 11, to retrieve the wind speed and direction from the WindSat 18-, 23-, and 37-GHz data. The sea surface temperature is from the monthly climatology [21]. The initial step ignores the wind direction effects and retrieves the wind speed, water vapor, and liquid water from  $T_v$  and  $T_h$  data using the isotropic model function for  $T_{V_{iso}}$  and  $T_{H_{iso}}$ . A conjugate gradient approach is used to search for the solution to minimize the sum of square (SOS) differences between the model and measured  $T_v$  and  $T_h$  data. The initial  $W$  and  $\tau$  estimates are then used together with the 18-GHz  $U$ , 18-GHz  $V$ , and 37-GHz  $U$  data to find the wind direction solutions that correspond to the local minimum of the SOS differences of  $U$  and  $V$  calculated from (2c) and (2d). In general, there are several local minima, yielding ambiguous

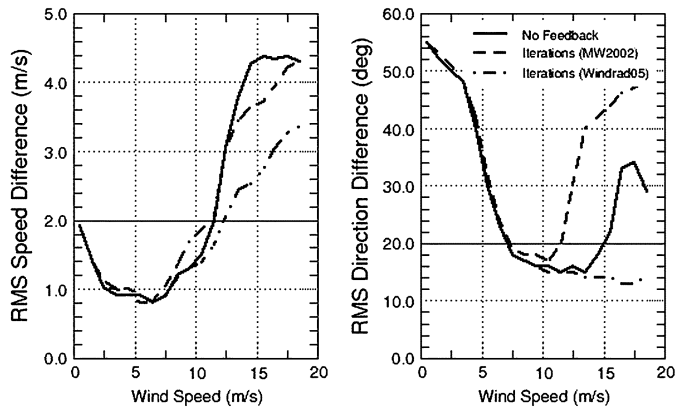


Fig. 12. RMS speed and direction difference between the NCEP GDAS winds and WindSat retrievals. The solid curves represent the wind speed retrieval from the WindSat 18- and 37-GHz  $T_v$  and  $T_h$  brightness temperatures using the AMSR model function [18] and the wind direction retrieved from the WindSat  $U$  and  $V$  channels provided the wind speed and  $\tau$  estimates from  $T_v$  and  $T_h$  data without iteration (no feedback). The dashed curves correspond to the iterated wind speed and direction estimates using the MW2002 directional model for  $T_v$  and  $T_h$  for iterations [13]. The dotted-dashed curves correspond to the iterated wind estimates using the Windrad05 directional model function for iterations.

wind direction solutions. For each directional ambiguity, the iterative approach reestimates the wind speed, WV, and LW from  $T_v$  and  $T_h$  data using the full model function with wind direction modulation. The updated  $W$  and  $\tau$  estimates are subsequently used to refine the direction of each ambiguity.

We apply the above wind retrieval algorithm to six months of WindSat data from September 2003 to February 2004. We started with the MW2002 directional model for  $T_v$  and  $T_h$  and the Windrad05 model for  $U$  and  $V$ . The retrievals are compared with the GDAS winds to indicate the impact of model function changes. After the initial wind speed and direction retrieval (no feedback), the root-mean-square (RMS) wind speed and direction differences for the closest directional ambiguity to the GDAS wind are illustrated in Fig. 12. The RMS wind speed differences reach as low as 1 m/s for 3–7-m/s GDAS wind speed, and rise above 4 m/s for 15–20-m/s wind speed. The RMS wind direction differences are below  $20^\circ$  for 7–15-m/s wind speeds. A significant part of the RMS wind speed or direction differences for high winds is due to the error in the GDAS analysis and the spatial and temporal mismatch with the WindSat observations.

After we iterate the wind speed and direction solution for the closest directional ambiguity three times using the approach described above, there is some minor improvement to the RMS wind speed difference for high winds near 15 m/s, but the RMS wind direction differences degrade significantly for greater than 12-m/s wind speeds. More iterations do not change the results. This suggests some deficiencies in the directional model function for  $T_v$  and  $T_h$ .

We repeated the same retrieval process using the WindRad05 directional model for  $T_v$  and  $T_h$ . Significant improvements to the RMS speed and direction differences are shown in Fig. 12. The RMS direction difference reduces to well below  $20^\circ$  for high winds, while the RMS wind speed difference is also reduced. This positive impact is clearly related to the changes of  $T_{v1}$  and  $T_{h2}$  model for above 15-m/s wind speeds. As we noted earlier the directional response in the MW2002 model is essentially an extrapolation for above 15-m/s wind speed. The extrap-

olation, resulting in significant underestimate of  $T_{v1}$ , apparently is inaccurate and introduces negative impact on the wind direction retrieval during iterations. The WindRad05 model with coefficients tuned by the limited WindRad measurements at high wind speeds (Fig. 6) produces more consistent results with the GDAS winds for above 15-m/s wind speed (Fig. 12). It is interesting to find that the wind direction retrievals from the WindSat 18–37-GHz channels can agree with the GDAS wind to about  $15^\circ$  or less for 7–20-m/s wind speeds.

Note that to infer the accuracy of WindSat retrievals from the RMS differences will require quantitative estimates of the GDAS accuracy. This is challenging because of the difficulty of finding an absolute anemometer reference for the error analysis of GDAS winds. An indirect assessment was made in [22] through the comparison with high-quality scatterometer winds and indicated the RMS wind speed differences of about 1–3 m/s between the GDAS and QuikSCAT winds, comparable to that between the GDAS and WINDSAT winds shown in the left panel of Fig. 12. If we assume that the GDAS, WindSat and QuikSCAT errors are all independent, the results suggest that the accuracy of WindSat wind speed is comparable to the accuracy of QuikSCAT scatterometer, about 1 m/s [22].

For the wind direction accuracy assessment, [22] shows that the standard deviation of the differences between the QuikSCAT and GDAS wind directions varies between  $20^\circ$  to  $23^\circ$  across the swath and also shows that the standard deviation of the directional difference between the QuikSCAT and the NDBC buoy winds is between  $10^\circ$  to  $20^\circ$  from 3 to 25 m/s. If we partition the difference equally into the QuikSCAT and NDBC buoy wind direction errors, the QuikSCAT direction error will be about  $7^\circ$  to  $15^\circ$  and consequently the standard deviation of the GDAS wind direction errors will be in the range of  $10^\circ$  to  $15^\circ$ . Subtracting the GDAS directional accuracy estimates from the RMS differences between the GDAS and WindSat wind directions suggests that WindSat has achieved  $10^\circ$  to  $15^\circ$  accuracy for greater than 7-m/s wind speed for the wind retrieval using the WindRAD05 model shown in Fig. 12. Our results appear to be consistent with the preliminary assessment of WindSat accuracy [23], which has shown comparison of the WindSat winds with the NDBC buoy and QuikSCAT winds.

## VI. SUMMARY

This paper summarizes the characteristics of WindSat polarimetric radiometer and airborne polarimetric radiometer and radar measurements acquired from the hurricane ocean wind experiment in 1997. The aircraft data indicated strongly correlated wind direction signatures in passive and active microwave observations of sea surfaces. Among the entire set of aircraft radar and radiometer measurements, the scatterometer signals,  $\sigma_{VV}$  and  $\sigma_{HH}$ , and the radiometer  $U$  and  $V$  data are fairly robust to weather conditions.

The aircraft data show that there are strong wind direction signals in polarimetric microwave sea surface brightness temperatures at wind speed up to 35 m/s. The wind direction signals are similar at 19 and 37 GHz.  $T_v$  and  $T_h$  data are sensitive to clouds with their wind directional dependence overwhelmed by inhomogeneous cloud covers. The third and fourth Stokes parameters,  $U$  and  $V$ , for high winds are fairly insensitive to

clouds, and have a wind directional dependence similar to those observed at moderate wind speeds (<12 m/s).

The WindSat data were collocated with the GDAS winds for directional analysis. The WindSat data are binned as a function of the GDAS wind speed and direction. There are clear wind direction signals in the WindSat polarimetric radiometer channels, except the 37-GHz *V* channel, for wind speed in the range of 5–22 m/s. Because of the lack of high wind analysis in the GDAS winds, the WINDSAT/GDAS collocations do not have sufficient wind direction samples for all wind directions for greater than 22-m/s wind speed.

We have reduced the Fourier coefficients from the JPL aircraft WINDRAD data and the spacecraft WindSat data. The WindSat data agree very well with the aircraft data, both showing rapid increase of directional signals with increasing wind speed from light to moderate wind speeds. The trend of WindSat data with the characteristics of decreasing second harmonics for high winds is consistent with the aircraft observations. We have used the WindSat and Windrad data to develop an empirical model function (WindRad05) to support the analysis and algorithm development for WINDSAT wind retrieval for 3–30-m/s wind speed. The retrieval analysis supports the consistency of the WindRad05 model function with the WindSat data.

#### ACKNOWLEDGMENT

The research carried out in this paper was performed by the Jet Propulsion Laboratory under Contract with the National Aeronautics and Space Administration. The authors are grateful to the WindSat project for providing the WindSat and GDAS matchup dataset.

#### REFERENCES

- [1] M. W. Spencer, C. L. Wu, and D. G. Long, "Improved resolution backscatter measurements with the seawinds pencil-beam scatterometer," *IEEE Trans. Geosci. Remote Sens.*, vol. 38, no. 1, pp. 89–104, Jan. 2000.
- [2] J. D. Kraus, *Radio Astronomy*, 2nd ed. Powell, OH: Cygnus-Quasar, 1986.
- [3] V. G. Irisov, A. V. Kuzmin, M. N. Pospelov, J. G. Trokhimovsky, and V. S. Etkin, "The dependence of sea brightness temperature on surface wind direction and speed. Theory and experiment," in *Proc. IGARSS*, Espoo, Finland, 1991, pp. 1297–1300.
- [4] M. S. Dzura, V. S. Etkin, A. S. Khrupin, M. N. Pospelov, and M. D. Raev, "Radiometers-polarimeters: Principles of design and applications for sea surface microwave emission polarimetry," in *Proc. IGARSS*, Houston, TX, 1992, pp. 1432–1434.
- [5] S. H. Yueh, W. J. Wilson, F. K. Li, W. B. Ricketts, and S. V. Nghiem, "Polarimetric measurements of sea surface brightness temperatures using an aircraft K-band radiometer," *IEEE Trans. Geosci. Remote Sens.*, vol. 33, no. 1, pp. 85–92, Jan. 1995.
- [6] —, "Polarimetric brightness temperatures of sea surfaces measured with aircraft K- and Ka-band radiometers," *IEEE Trans. Geosci. Remote Sens.*, vol. 35, no. 5, pp. 1177–1187, Sep. 1997.
- [7] S. H. Yueh, W. J. Wilson, S. Dinardo, and F. K. Li, "Polarimetric microwave brightness signatures of ocean wind directions," *IEEE Trans. Geosci. Remote Sens.*, vol. 37, no. 2, pp. 949–959, Mar. 1999.
- [8] J. R. Piepmeier and A. J. Gasiewski, "High-resolution passive polarimetric microwave mapping of ocean surface wind vector fields," *IEEE Trans. Geosci. Remote Sens.*, vol. 39, no. 3, pp. 606–622, Mar. 2001.
- [9] B. Laursen and N. Skou, "Wind direction over the ocean determined by an airborne, imaging, polarimetric radiometer system," *IEEE Trans. Geosci. Remote Sens.*, vol. 39, no. 7, pp. 1547–1555, Jul. 2001.
- [10] J. Lahtinen, J. Pihlflyckt, K. Mononen, S. J. Tauriainen, M. Kempainen, and M. T. Hallikainen, "Fully polarimetric microwave radiometer for remote sensing," *IEEE Trans. Geosci. Remote Sens.*, vol. 41, no. 8, pp. 1869–1878, Aug. 2003.
- [11] S. H. Yueh, "Modeling of wind direction signals in polarimetric sea surface brightness temperatures," *IEEE Trans. Geosci. Remote Sens.*, vol. 35, no. 6, pp. 1400–1418, Nov. 1997.
- [12] F. J. Wentz, "Measurement of oceanic wind vector using satellite microwave radiometers," *IEEE Trans. Geosci. Remote Sens.*, vol. 30, no. 5, pp. 960–972, Sep. 1992.
- [13] T. Meissner and F. Wentz, "An updated analysis of the ocean surface wind direction signal in passive microwave brightness temperatures," *IEEE Trans. Geosci. Remote Sens.*, vol. 40, no. 6, pp. 1230–1240, Jun. 2002.
- [14] S. H. Yueh, R. West, F. Li, W.-Y. Tsai, and R. Lay, "Dual-polarized ku-band backscatter signatures of hurricane ocean winds," *IEEE Geosci. Remote Sens.*, vol. 38, no. 1, pp. 73–88, Jan. 2000.
- [15] P. W. Gaiser, K. M. St. Germain, E. M. Twarog, G. A. Poe, W. Purdy, D. Richardson, W. Grossman, W. L. Jones, D. Spencer, G. Golba, J. Cleveland, L. Choy, R. M. Bevilacqua, and P. S. Chang, "The WindSat spaceborne polarimetric microwave radiometer: Sensor description and early orbit description," *IEEE Trans. Geosci. Remote Sens.*, vol. 42, no. 11, pp. 2347–2361, Nov. 2004.
- [16] S. H. Yueh, R. Kwok, and S. V. Nghiem, "Polarimetric scattering and emission properties of targets with reflection symmetry," *Radio Sci.*, vol. 29, no. 6, pp. 1409–1420, Nov.–Dec. 1994.
- [17] F. J. Wentz, "A well-calibrated ocean algorithm for Special Sensor Microwave/Imager," *J. Geophys. Res.*, vol. 102, no. C4, pp. 8703–8718, Apr. 1997.
- [18] F. J. Wentz and T. Meissner, "AMSR ocean algorithm, Version 2, Algorithm Theoretical Basis Document," Remote Sens. Syst., Santa Rosa, CA, RSS Tech. Rep. 121599A-1, Nov. 2000.
- [19] H. J. Liebe, "An updated model for millimeter wave propagation in moist air," *Radio Sci.*, vol. 20, no. 5, pp. 1069–1089, 1985.
- [20] F. J. Wentz, M. H. Freilich, and D. K. Smith, "NSCAT-2 geophysical model function," presented at the 1998 Fall AGU Meeting, San Francisco, CA, 1998.
- [21] R. W. Reynolds and T. M. Smith, "A high resolution global sea surface temperature climatology," *J. Clim.*, vol. 8, pp. 1571–1583, 1995.
- [22] D. B. Chelton and M. H. Freilich, "Scatterometer-based assessment of 10-m wind analyzes from the operational ECMWF and NCEP numerical weather prediction models," *Mon. Weather Rev.*, vol. 133, pp. 409–429, 2005.
- [23] M. Freilich and B. Vanhoff, "The accuracy of preliminary WindSat vector wind measurements: Comparisons with NDBC buoys and QuikSCAT," *IEEE Trans. Geosci. Remote Sens.*, vol. 44, pp. 622–637, Mar. 2006.



**Simon H. Yueh** (M'92–SM'01) received the S.B. and S.M. degrees from the National Taiwan University, Taipei, Taiwan, R.O.C., in 1982 and 1984, respectively, and the Ph.D. degree in electrical engineering from the Massachusetts Institute of Technology (MIT), Cambridge, in 1991.

He was a Postdoctoral Research Associate at MIT from February to August 1991. In 1991, he joined the Radar Science and Engineering Section, Jet Propulsion Laboratory (JPL), Pasadena, CA, and worked as a Radar System Engineer for the SIR-C, NSCAT, and

SeaWinds missions. He is the supervisor of a radar system engineering and algorithm development group and is a Principal Engineer at JPL. He led the Aquarius instrument team for a successful National Aeronautics and Space Administration (NASA) Earth System Science Pathfinder mission proposal. He has been the Principal/Co-Investigator of numerous research projects, including the polarimetric wind radiometer research, the NUSCAT project for hurricane wind measurements, the Passive/Active L-/S-band (PALS) radiometer and radar project, the NASA Instrument Incubator Project for a mission concept using a large mesh-deployable antenna for soil moisture and ocean salinity sensing, the airborne polarimetric radar (POLSCAT) for ocean wind velocity measurements, the POLSCAT/Cold Land Process Experiment in 2002–2004, and the Advanced Component Technology lightweight dual-frequency antenna feed project. He is leading the development of the Cold Land Process Pathfinder mission concept at JPL. He also serves on the Cold Land Process Working Group, Salinity Sea Ice Working Group, Ocean Vector Wind Science Team, and WINDSAT Science Team. He has authored four book chapters and published 52 refereed articles and more than 100 conference presentations. His current fields of interest include techniques and instrument developments for microwave remote sensing of soil moisture, ocean surface salinity, ocean winds and polar ice, and theories for active and passive microwave remote sensing. He is an Associate Editor of *Radio Science*.

Dr. Yueh received the IEEE GRSS Transactions Prize Paper Award in 1995, the JPL Lew Allen Award in 1998, the IEEE IGARSS 2000 Best Paper Award, the JPL Ed Stone Award in 2002, and IEEE GRSS Transactions Prize Paper Award in 2002. He is a member of the American Geophysical Union.



**William J. Wilson** (S'59–M'64–SM'86–F'98) received the B.S.E.E. degree from the University of Washington, Seattle, in 1961, and the M.S.E.E., E.E., and Ph.D. degrees in electrical engineering from the Massachusetts Institute of Technology, Cambridge, in 1963, 1964, and 1970, respectively.

He is currently a Senior Research Scientist at the National Aeronautics and Space Administration Jet Propulsion Laboratory (JPL), Pasadena, CA. In 1964, he served in the U.S. Air Force, working on military communication satellites. In 1970, he joined the Aerospace Corporation, Los Angeles, CA, and was involved in the design and construction of the millimeterwave receivers and radio astronomy observations. In 1976–1977, he was an Assistant Professor in the Electrical Engineering Department, University of Texas, Austin. He returned to Aerospace Corporation in 1977, where he was involved with research in millimeterwave radiometers and low-noise receivers. In 1980, he joined the staff of JPL, and is the Supervisor of the Microwave Advanced Systems Group. At JPL, he has been working on low-noise microwave and millimeterwave radiometers and radar systems for aircraft and spacecraft for Earth remote sensing applications. He is currently working on the Aquarius ocean salinity mission, development of ultrastable microwave radiometers, and the GeoStar Geosynchronous microwave-sounding instrument. He has published more than 160 technical papers and reports.



**Steve J. Dinardo** (M'95) received the B.S.E.E. degree from California State University, Los Angeles, in 1983.

He is currently a Senior Engineer at the National Aeronautics and Space Administration (NASA) Jet Propulsion Laboratory (JPL), Pasadena, CA. He joined NASA JPL in 1978. At JPL, he has been involved in various projects, including very long base interferometry (VLBI), mobile VLBI, orbiting VLBI, GPS receiver development, and international GPS service. From 1995 through 1997, he was responsible for the deployment of the JPL aircraft polarimetric wind radiometers (WINDRAD) on NASA's DC-8 and P-3 aircraft. He successfully coordinated the Hurricane Ocean Wind Experiment, sponsored by NASA and NPOESS, resulting in the first airborne Ku-band scatterometer and multi-frequency polarimetric radiometers flights over hurricanes. He has also been responsible for development and deployment of JPL's aircraft rain radar and a 94-GHz cloud profiling radar on NASA's DC-8. He built the JPL Ku-band Polarimetric Scatterometer (POLSCAT), deployed on the NCAR C-130, for the first successful demonstration of polarimetric wind scatterometer technique. He has been responsible for the deployment of POLSCAT and WINDRAD on the DC-8 to support the NASA Cold Land Process Experiment in 2002–2003. He is currently involved in the development of low-noise microwave radiometers and radar systems for aircraft and spacecraft for remote sensing of soil moisture and ocean salinity.



**S. Vincent Hsiao** received the B.S. and M.S. degrees from the National Taiwan University, Taipei, Taiwan, R.O.C., in 1970 and 1972, respectively, and the Ph.D. degree in engineering sciences from the University of Florida, Gainesville, in 1978.

His interests are in various aspects of ocean remote sensing, including science, engineering, algorithms, and data processing. His previous and current work involves the Projects of NSCAT, TOPEX, QSCAT, SEAWINDS, etc.